RETENTION OF PROGRAMMABLE METALLIZATION CELLS DURING IONIZING RADIATION EXPOSURE

by

Jennifer Lynn Taggart

A Thesis Presented in Partial Fulfillment
of the Requirements for the Degree
Masters of Science

Approved April 2015 by the
Graduate Supervisory Committee:

Hugh Barnaby, Chair
Michael Kozicki
Keith Holbert

ARIZONA STATE UNIVERSITY

May 2015

©2015 Jennifer Lynn Taggart
All Rights Reserved

ABSTRACT

Non-volatile memory (NVM) has become a staple in the everyday life of consumers. NVM manifests inside cell phones, laptops, and most recently, wearable tech such as smart watches. NAND Flash has been an excellent solution to conditions requiring fast, compact NVM. Current technology nodes are nearing the physical limits of scaling, preventing Flash from improving. To combat the limitations of Flash and to appease consumer demand for progressively faster and denser NVM, new technologies are needed. One possible candidate for the replacement of NAND Flash is programmable metallization cells (PMC). PMC are a type of resistive memory, meaning that they do not rely on charge storage to maintain a logic state. Depending on their application, it is possible that devices containing NVM will be exposed to harsh radiation environments. As part of the process for developing a novel memory technology, it is important to characterize the effects irradiation has on the functionality of the devices.

This thesis characterizes the effects that ionizing γ-ray irradiation has on the retention of the programmed resistive state of a PMC. The PMC devices tested used $Ge_{30}Se_{70}$ doped with Ag as the solid electrolyte layer and were fabricated by the thesis author in a Class 100 clean room. Individual device tiles were wire bonded into ceramic packages and tested in a biased and floating contact scenario.

The first scenario presented shows that PMC devices are capable of retaining their programmed state up to the maximum exposed total ionizing dose (TID) of 3.1 Mrad(Si). In this first scenario, the contacts of the PMC devices were left floating during exposure. The second scenario tested shows that the PMC devices are capable of retaining their state until the maximum TID of 10.1 Mrad(Si) was reached. The contacts in the second scenario were biased, with a 50 mV read voltage applied to the anode contact. Analysis of the results show that $Ge_{30}Se_{70}$ PMC are ionizing

radiation tolerant and can retain a programmed state to a higher TID than NAND Flash memory.

Dedicated to my Fiancé

William Alexander Johnson

ACKNOWLEDGEMENTS

I would first like to thank my research adviser, Dr. Hugh Barnaby, for providing me this opportunity to do radiation effects research as well as allowing me to get hands on experience in device fabrication. Dr. Barnaby's show of excitement toward this research as well has his great patience has been inspiring. I would also like to thank my committee member Dr. Michael Kozicki for never allowing his classes or lab meetings to be boring and for allowing me access to his great depth of knowledge concerning resistive memory. I would like to thank my other committee member Dr. Keith Holbert for the use of his irradiation laboratory and for taking the time to answer my emails. I want to thank Mehdi Saremi for providing the electric field simulation results presented in this thesis. I also thank Yago Gonzalez-Velo for always being around when I needed help with my research and for being a good friend.

Concerning my internship at Sandia National Laboratories, I would like to thank Michael McLain, Fred Hartman, and Matthew Marinella for allowing me to have this fun and fantastic opportunity. I would especially like to thank my mentor Michael McLain, who allowed me my own opportunities to experience failure and success. I would like to thank Don Hanson and Maryla Wasiolek for supporting my testing at the Gamma Irradiation Facility. I would also like to thank Ed Bielejec as well as the rest of the staff at the Sandia Ion Beam Laboratory for allowing me access to their ion beams and for providing me with insight toward my future PhD studies.

TABLE OF CONTENTS

Page

LIST OF TABLES . . . vi

LIST OF FIGURES . . . vii

CHAPTER

1 INTRODUCTION . . . 1

1.1 The Future of Non-Volatile Memory . . . 1

1.2 Motivation . . . 3

1.3 Thesis Outline . . . 3

2 DEVICE OPERATION AND FABRICATION . . . 5

2.1 What is Resistive Memory? . . . 5

2.2 Fundamentals of Programmable Metallization Cells . . . 5

2.3 Device Programming and I-V Characteristics . . . 9

2.4 Retention of State . . . 11

2.5 Fabrication . . . 13

2.6 Ag Doping Profile in PMC Structures . . . 19

3 IONIZING RADIATION EFFECTS . . . 22

3.1 Ionizing Radiation Effects in Semiconductors . . . 22

3.2 Effect of the Electric Field on PMC Retention . . . 23

4 RETENTION DURING ^{60}Co γ-RAY EXPOSURE . . . 28

4.1 State Retention During Ionizing Irradiation to 3.1 Mrad(Si) . . . 28

4.2 State Retention During Ionizing Irradiation to 10.1 Mrad(Si) . . . 34

4.3 Discussion and Analysis . . . 39

5 CONCLUSION . . . 42

REFERENCES . . . 44

LIST OF TABLES

Table Page

2.1 Resistive Memory Technologies 6

3.1 Material Parameters Used to Model PMC 23

3.2 Dose Rates and Equivalent Generation Rates 23

4.1 Radiation Dose Steps 30

LIST OF FIGURES

Figure Page

1.1 Commercial IoT Devices Currently in the Market. 2

2.1 Cross Section of a Vertical PMC Stack Showing the Creation and Dissolution of the Conductive Filament. 7

2.2 Filament Growth Between the Ag Anode and Pt Cathode of a lateral Pt/H_2O/Ag Cell. 9

2.3 Measured I-V Characteristics of a PMC. 10

2.4 PMC Programming and Erasing with Pulsed Signals. 11

2.5 Extrapolated Ten Year Retention of PMC Using the Arrhenius Relation. 12

2.6 Retention of PMC Devices at Room Temperature, Programmed with Various Compliance Currents. 13

2.7 Deposition of 100 nm SiO_2. 14

2.8 Deposition of 100 nm Ni. 14

2.9 First Lithography Mask Exposure to Create Cathode Bar. 15

2.10 Ni Layer Wet Etched to Create Cathode Bar Followed by Deposition of SiO_2. 15

2.11 Second Lithography Mask to Etch Via Through SiO_2. 16

2.12 Vias Wet Etched Through SiO_2 to Ni Layer. 17

2.13 Third Lithography Mask for Device Layer Lift-Off. 17

2.14 $Ge_{30}Se_{70}$ is Deposited Followed by Ag. 17

2.15 $Ge_{30}Se_{70}$ is Photo-Doped with Ag by Exposing to UV Light. 18

2.16 Additional Ag is Deposited Then the Wafer is Soaked in Acetone to Remove the Resist and Lift-Off the Excess Material. 18

2.17 Al is Deposited and Lifted Off to Create Top Anode Crossbar. 19

Figure Page

2.18 Fabricated Crossbar Tile. Zoomed Image Highlights the Device Contacts and Active Device Region. 19

2.19 EDS Data Showing the Profile of Ag Throughout a PMC. 20

2.20 Ag Doping Regions in the $Ge_{30}Se_{70}$ Layer (Left) with the Equivalent RC Circuit Network (Right). 20

3.1 Forces Acting Upon the Filament. 24

3.2 Electric Field Through a PMC in HRS for Multiple Generation Rates. . 25

3.3 Electric Field Through a PMC in LRS for multiple Generation Rates. . 25

3.4 Equal Potential and Electric Field Vectors for the LRS During a) No Irradiation and b) Irradiation with a Generation Rate of 10^{31} $cm^{-3}s^{-1}$. 26

3.5 Equal Potential and Electric Field Vectors for a Generation Rate of $10^{17}cm^{-3}s^{-1}$. 27

4.1 Crossbar Device Tile Wire Bonded Into a 28-pin CDIP. 29

4.2 Test Fixture Used for Performing Automated Electrical Measurements. 30

4.3 The Gammacell 220 Used for γ-Ray Exposure. Photo Provided By Dr. Keith Holbert. 31

4.4 The Source Ring Inside the Central Chamber of the Gammacell 220, as Depicted in the Gammacell 220 Instruction Manual. 31

4.5 Board with Marked Dose Contours of the Gammacell 220 Chamber. . . . 32

4.6 Retention of PMC Devices During Ionizing γ-Ray Irradiation to a TID of 3.1 Mrad(Si). 33

4.7 Dry-Cell at GIF with Raised ^{60}Co Source Ring. Original Photo Taken by Randy Montoya. 35

4.8 Circuit Configuration Used to Actively Monitor PMC Devices. 36

Figure Page

4.9 Retention of Programmed Resistances up to a TID of 10 Mrad(Si). 37
4.10 Retention of the HRS. 38
4.11 Retention of the LRS. 38
4.12 Percent Errors as a Function of TID in NAND Flash No Refresh Mode Retention. 41

Chapter 1

INTRODUCTION

1.1 The Future of Non-Volatile Memory

If you open up a modern day computer, chances are you will find a solid-state hard drive inside. Over the past decade, NAND Flash memory has dominated the non-volatile memory (NVM) industry in the form of hard drives, USB thumb drives, and memory cards. Consumers choose Flash devices because of their small size and fast read and write times. Flash memory is found inside smartphones and other handheld electronics that have become essential to everyday living. With the emerging concept of the Internet of Things (IoT), common household items such as air conditioners, cars, running shoes, and even the cup we drink out of [1], will be embedded with sensors and NVM to store the collected data. Many of these devices are small wearables designed to be unobtrusive and fashionable, as shown in Fig. 1.1, and thus provide very limited space for electronic components.

While Flash memory has been a staple of modern electronics and has increased in speed and storage size over the past decade, complementary metal-oxide semiconductor (CMOS) feature size, which essentially defines the speed and size of Flash memory devices, will soon be reaching its physical limits [7]. The limitations on transistor feature size will therefore hinder further improvement of Flash memories in terms of performance and increased density. To continue advancement in technology performance as dictated by Moore's Law, new materials, methods, and technologies need to be developed to replace or supplement CMOS and the impending physical barriers associated with modern CMOS processing [8]. Many new materials and fabrication

Figure 1.1: Commercial IoT devices currently in the market [2],[3],[4],[5],[6].

techniques are being researched by industry and university laboratories to combat the limitations of CMOS. The International Technology Roadmap for Semiconductors (ITRS) has dubbed this new research trend as "More-than-Moore" [7]. Several novel technologies have been identified as promising alternatives to flash memories. Many of the new memory offerings deviate from the transistor method of charge storage and exploit measurable changes in material properties. Among these is a technology known generally as electrochemical metallization (ECM) memory [9], also known as programmable metallization cell (PMC) [10], and in the context commercial of memory arrays, conductive bridge random access memory (CBRAM) [11]. PMCs rely on electrochemical metallization, where metal is driven through a solid electrolyte layer to create a low resistance filament when a voltage is applied [12]. The resistance of the filament can be controlled by adjusting bias conditions. When the bias is removed, the filament will remain. The filament can be dissolved by reversing the

bias, reversing the electrochemical reaction.

1.2 Motivation

PMC memory has the potential to scale to smaller feature sizes, has even faster read and write times and requires less energy than Flash. The typical read and write times for NAND Flash is in the order of 100 μs [7] whereas PMCs have read and write times occurring within tens of nanoseconds [13]. Possessing the ability to scale to smaller dimensions means that future memory arrays can be made larger and or occupy less space on a chip. Smaller devices with larger storage capacity are extremely beneficial in devices, like medical implants, wearable electronics, satellites, and space research vehicles, where each cubic millimeter of space is valuable real estate. An important consideration for many of these devices is how they will holds up after radiation exposure. Devices used in small hand-held electronics have the potential of being exposed to X-rays from airport baggage scanners. Components used in medical implants sometimes undergo sterilization using ^{60}Co γ-ray irradiation up to tens of Mrad [14]. Devices that operate outdoors are exposed to UV radiation from the Sun; and if operating in space, they can be damaged by high energy solar particles and cosmic rays. In all the aforementioned scenarios, it would be a waste of time and money for the consumer, should devices cease to function after exposure to ionizing radiation. The ionizing radiation tolerance of PMC devices needs to be studied to evaluate the functionality of these devices in harsh radiation environments.

1.3 Thesis Outline

This thesis will explore the effects ionizing radiation has on the retention of PMC devices. Chapter 2 of this thesis provides a brief overview of the PMC operation mechanisms as well as describes the methods used for fabricating the devices used for

total ionizing dose (TID) testing. Chapter 3 explores the effect ionizing radiation has on the intrinsic electric field of the PMC. Chapter 4 presents the effects ionizing γ-ray irradiation has on the retention of PMC devices. The results show that PMC devices have excellent retention during γ-ray exposure. Chapter 5 presents a summary of results and a conclusion.

Chapter 2

DEVICE OPERATION AND FABRICATION

2.1 What is Resistive Memory?

Resistive switching or resistive memory is a term used to describe several memory technologies currently in development as a supplement and possibly an alternative to current solid-state memory technologies. A resistive memory cell is a device whose digital state is dictated by the resistance across the device. The resistance can be reliably reprogrammed to a desired resistance value $>10^4$ times, the standard for comparison against NAND Flash devices [7]. Several resistive memory technologies exist, namely programmable metallization cells (PMC), phase-change memory (PCM), and valence change memory (VCM) [15]. Each technology relies on unique mechanisms to create changes in the resistive state. Table 2.1 presents a brief list of resistive switching technologies and mechanisms.

2.2 Fundamentals of Programmable Metallization Cells

Programmable metallization cells (PMC) are a resistive switching technology invented and developed by Dr. Michael Kozicki at Arizona State University. A PMC consists of a simple metal-electrolyte-metal structure. In a typical vertical structure, as shown in Fig. 2.1, the bottom metal electrode is formed from an inert metal such as nickel, tungsten, or platinum. Several different metal doped chalcogenides can be used for the solid electrolyte layer such as Cu-SiO_2, Ag-Ge_xSe_{1-x}, or Ag-Ge_xS_{1-x}. The top metal consists of a thin layer of the same active metal (Au or Cu) used to dope the chalcogenide layer.

Table 2.1: Resistive Memory Technologies

Memory Type	Typical Materials	Programming Mechanism
Programmable metalization cells	Solid electrolytes of metal doped chalcogenides: Cu-SiO_2 [16], Ag-Ge_xSe_{1-x} [17], [18], [19], or Ag-Ge_xS_{1-x} [20]	Active metal layer is oxidized when a positive voltage is applied. Metal cations drift along applied electric field and reduce on inert metal cathode to build a low resistance filament. Resistive state is dependent on thickness of metal filament.
Valence change memory	Metal oxides such as: TaO_x [21], TiO_2 [22], HfO_2 [23]	Applying a voltage oxidizes metal oxide region. Oxygen ions percolate out of active region, leaving behind a conductive path between electrodes.
Phase change memory	$Ge_2Sb_2Te_5$ [24]	Chalcogenide layer is changed between amorphous and crystalline phases using a current driven heating element. Crystalline state possesses a lower resistance than the amorphous state.

The functionality of PMC devices relies on a mechanism known as electrochemical metallization (ECM). During ECM, oxidation and reduction (redox) reactions result in the growth of a metallic filament. During oxidation, a neutral metal M is striped of an electron, resulting in a positively charged ion, as described by the reaction equation (2.1). When metal M is reduced, reaction equation (2.2), the ion gains an electron, becoming a neutral metal atom once more. In a simplistic form, a non-programmed PMC device can be thought of as a parallel plate capacitor whose electric field is represented by the relation (2.3), with constant voltage V applied across the device and a distance d between the anode and cathode. When a voltage bias is applied to the anode, the active metal in the anode oxidizes and travels along the electric field

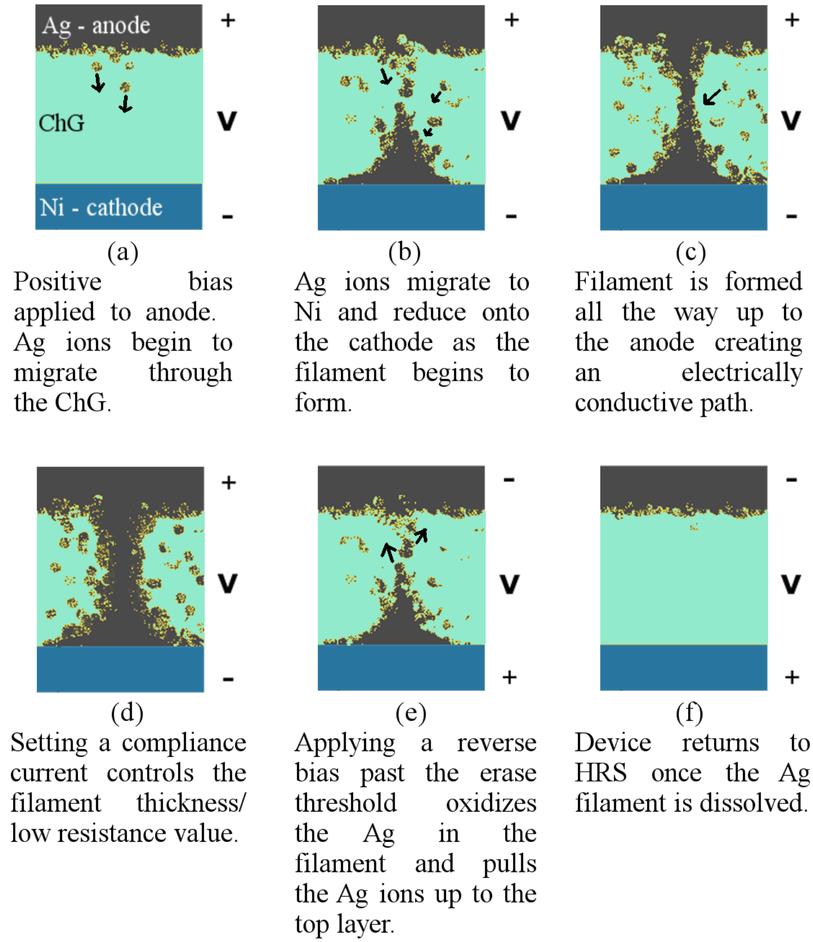

Figure 2.1: Cross section of a vertical PMC stack showing the creation and dissolution of the conductive filament.

to the cathode, as depicted in Fig. 2.1(a). At the cathode, the metal cation reduces to become a metallic metal deposited on the cathode. As metal deposits onto the cathode, the distance d between the anode and effective cathode decreases, resulting in an increase of the electric field across the PMC for a fixed bias. The increase in the electric field causes more metal cations in the electrolyte to migrate toward the metal electrodeposit, shown in Fig. 2.1(b).

$$M \rightarrow M^{+} + e^{-} \tag{2.1}$$

$$M^+ + e^- \rightarrow M \tag{2.2}$$

$$E \propto \frac{V}{d} \tag{2.3}$$

Maintaining the bias for several nanoseconds [20] will result in the growth of a conductive filament (CF) spanning the gap between the anode and cathode contacts as shown in Fig. 2.1(c). The actual time for CF growth depends on the magnitude of applied voltage as well as temperature. Characterization of CF growth as a function of voltage has been measured and modeled in [20], [25], and [26]. Applying a bias beyond the filament creation time will result in a thickening of the CF, as shown in Fig. 2.1(d), decreasing the resistance across the device. The resistance of the CF can be modeled as a conic structure with its base widest at the cathode [27]. Equation (2.4) provides a simplistic model of how the CF resistance R_{CF} decreases as a function of CF radii, where r_a radius at the anode contact and r_c radius at the cathode contact, and ρ is the resistivity of the filament [27]. Mathematically this simple conic structure can appropriately model the conduction across a CF but the actual structure of the filament is a dendrite with a thick base at the cathode and thin limbs reaching toward the anode [28]. Observed filament structures are featured in Fig. 2.2.

$$R_{CF} = \frac{\rho d}{\pi r_a r_c} \tag{2.4}$$

By reversing the bias applied between the anode and cathode, the ECM process is reversed. With a reverse bias applied, the filament will oxidize and the ionized metal in the filament will drift back to the active metal anode as shown in Fig. 2.1(e). The resistance across the device will be restored near to the original high resistance state (HRS) once the CF is dissolved (Fig. 2.1(f)).

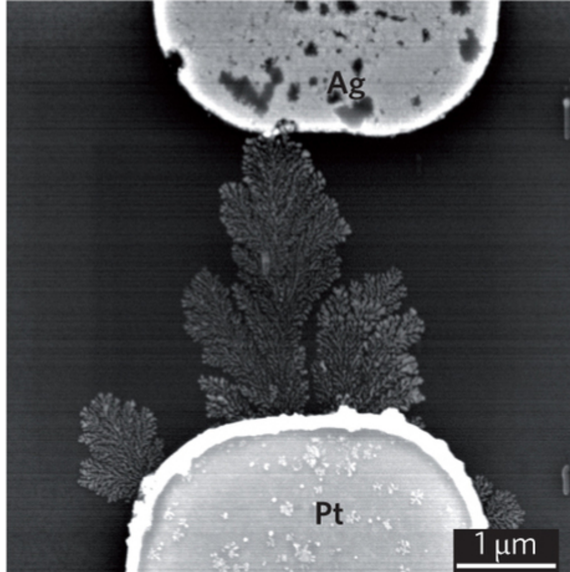

Figure 2.2: Filament growth between the Ag anode and Pt cathode of a lateral Pt/H_2O/Ag cell [28]. Reprinted with permission ©2007, AIP Publishing LLC.

2.3 Device Programming and I-V Characteristics

The PMCs studied in this thesis consist of an inert metal cathode made of nickel, under a layer of $Ge_{30}Se_{70}$ chalcogenide glass (ChG) doped with Ag and topped with a layer of Ag for the active metal anode. A representation of the device stack is shown in Fig. 2.1a.

Fig. 2.3 shows a typical current-voltage (I-V) curve for the program and erasure of a PMC device. The programming curve (red dash-dotted line) was created by sweeping the voltage across the device from 0 V to 0.5 V and back to 0 V. A device initially in the HRS will abruptly switch to the low resistance state (LRS) at some threshold. This threshold can vary from device to device but is typically observed to occur between 150 mV and 300 mV, as shown in Fig. 2.3. The applied current is capped by a specified compliance current. In the case of Fig. 2.3, this compliance is 1 μA. When considering the sweep from 0.5 V back to 0 V, the inverse slope of the curve highlights the programmed resistance state of the device. The erasure curve

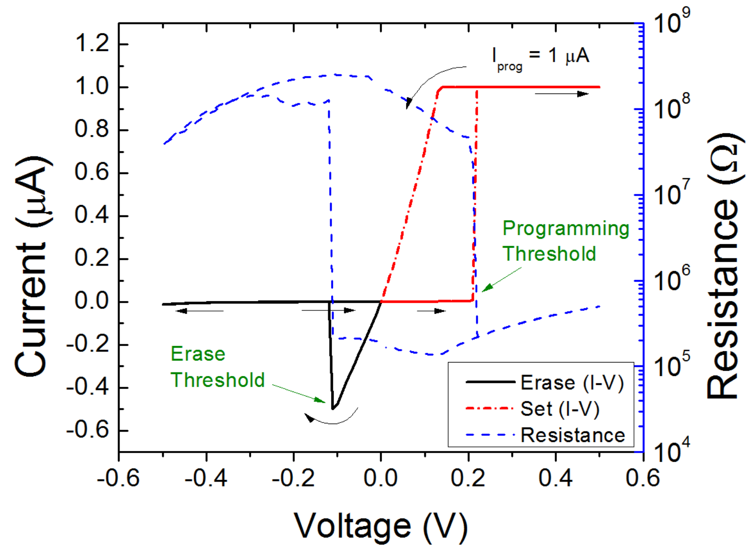

Figure 2.3: Measured I-V characteristics of a PMC.

(black solid line) was created by sweeping from 0 V to -0.5 V then back to 0 V. For a device initially in a LRS, after reaching a threshold of approximately -100 mV, the filament will begin to dissolve resulting in a HRS. The sweep from -0.5 V to 0 V shows that the device remains in the HRS after being erased. The dashed blue line shows how the resistance of the PMC changes from a high resistance to a low resistance as the device is set and reverts back to a high resistance when the voltage reaches the erase threshold.

PMC devices can also be programmed using a pulsed signal instead of relying on compliance current to regulate the state [26], [29], [30]. Fig. 2.4 shows the response of a PMC to a square wave pulse. Once the filament establishes a continuous connection, the filament resistance will continue to decrease until the voltage is removed. By regulating the pulse width, the resistance state of the device can be controlled. The speed at which the filament forms can also be manipulated by adjusting the amplitude of the pulse [26].

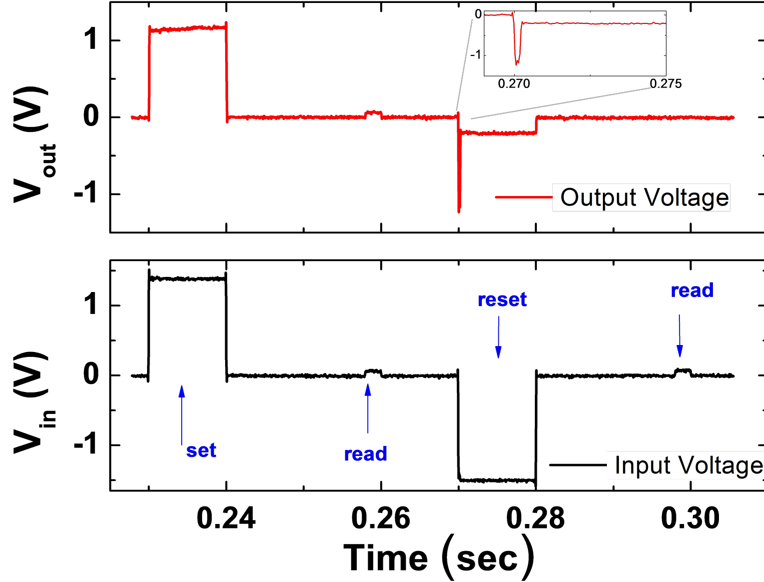

Figure 2.4: PMC programming and erasing with pulsed signals [30]. The bottom plot is the pulse train used for programming and the bottom plot displays the response of the PMC. Reprinted with permission ©2014 IEEE.

2.4 Retention of State

Retention of the programmed logic state is a common figure of merit and a necessary parameter to be characterized when developing NVM. Retention testing involves programming an individual memory cell or an array to a fixed logic state and observing how long the state is maintained. The status of the cell is tested periodically to determine the state's evolution over time. Current Flash memory has a projected retention of ten years or more [7], [31]. It is not practical to observe the real time retention over a ten year period. Methods are employed to accelerate the deterioration of the state and relate the result to an equivalent time during normal operation. A common method of accelerated testing involves performing retention tests at elevated temperatures [31], [32]. Instead of applying a temperature stress, a small continuous voltage can also be applied to degrade the state as shown in Fig. 2.5 [33], [34].

$$t = Ae^{E_a/k_B T} \tag{2.5}$$

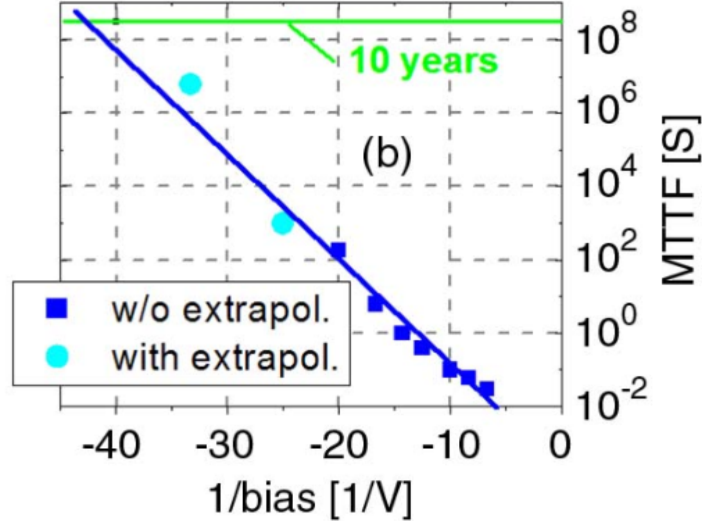

Figure 2.5: Extrapolated ten year retention of PMC using the arrhenius relation [33]. Reprinted with permission ©2009 IEEE.

The retention under normal operating conditions is extracted from the stressed retention results using the Arrhenius relation (2.5) where t is the retention time, A is a prefactor that can be extracted from measured results, E_a is the activation energy, k_B is Boltzmann's constant, and T is the temperature. The retention time t is plotted versus the $1/T$ relation to temperature. When plotting voltage stress measurements, the k_BT term can be replaced with $-qV$ as shown in Fig. 2.5.

For PMC devices, the retention has been shown to be largely dependent upon the initial resistance state. The results from Russo, *et al.* in Fig. 2.6 show how devices programmed at a lower compliance current become unstable and begin to decay to a higher resistance state sooner than devices programmed with higher compliance currents [26]. The next chapter of this thesis will examine the effects ionizing radiation has on the retention of PMCs.

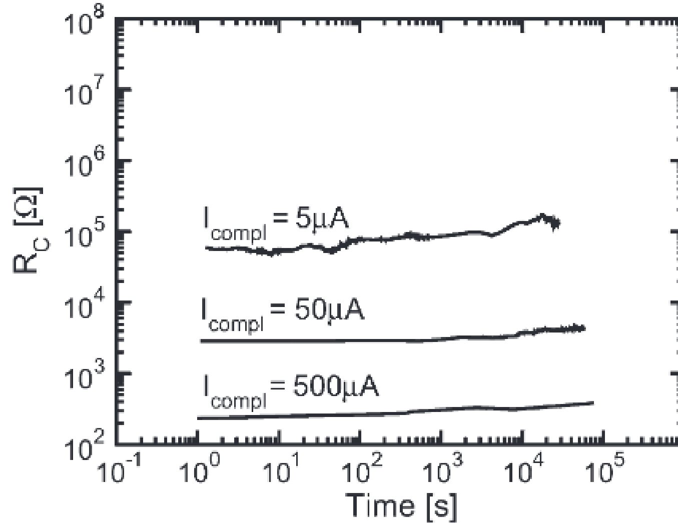

Figure 2.6: Retention of PMC devices at room temperature, programmed with various compliance currents [26]. Reprinted with permission ©2009 IEEE.

2.5 Fabrication

All PMC devices used in the following experiments were fabricated at Arizona State University in the NanoFab class 100 cleanroom facility operated by the Center for Solid State Electronics Research. The full fabrication process is highlighted in Fig. 2.7 - 2.17. A four inch diameter, 525 μm thick Si p-type wafer was placed inside a Lesker PVD75 electron-beam evaporator. After reaching a vacuum of approximately 3×10^{-6} torr, a 100 nm layer of SiO_2 was deposited at 0.9 Å/s to provide insulation between the Si substrate and the device structures (Fig. 2.7). Without breaking vacuum, a 100 nm layer of Ni was deposited at 0.9 Å/s on top of the SiO_2 insulating layer, shown in Fig. 2.8. After Ni deposition, the vacuum chamber was brought back up to atmosphere and the wafer removed.

To create the nickel (Ni) contact patterning, hexamethyldisilazane (HMDS) was first spun onto the nickel surface to promote adhesion of the resist. HMDS was always applied before spinning on resist, though this step will not be mentioned in further

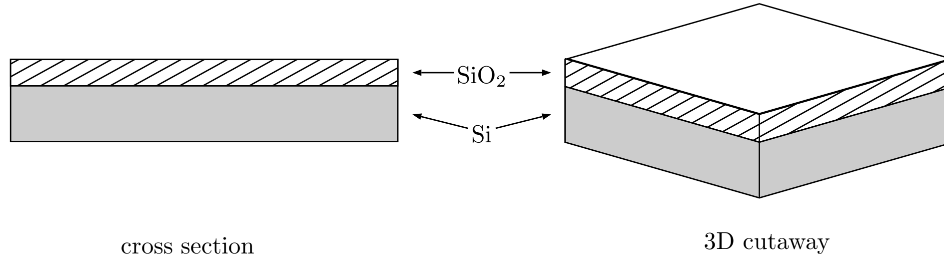

Figure 2.7: Deposition of 100 nm SiO_2.

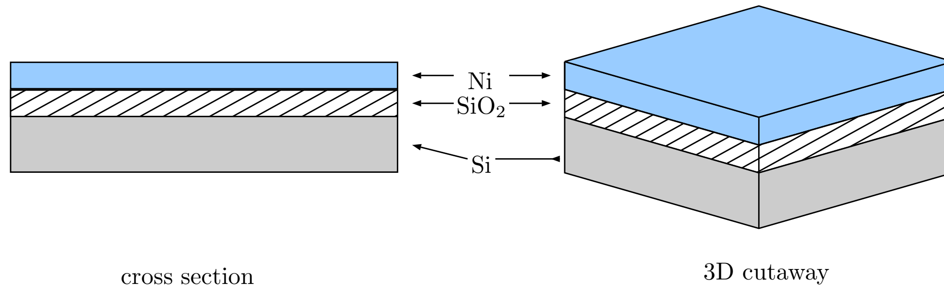

Figure 2.8: Deposition of 100 nm Ni.

lithography steps. A 1 μm layer of AZ3312 photoresist was spun onto the treated nickel surface at 3500 RPM for 30 seconds. The resist covered wafer was then soft baked at 100°C for 60 seconds. Lithography exposure was performed using an EVG 620 set to 45 mJ/cm^2 UV exposure. Mask #1 was used to create the Ni cathode bar positive image in the resist (Fig. 2.9). After exposure, the resist was developed for 80 seconds using AZ 300 MIF developer. Preparation of the resist layer for wet etching was concluded by hard baking the wafer for three minutes at 110°C. The Ni left exposed after lithography was etched away after ten minutes, using 100 mL of Nickel Etchant TFB (Nitric Acid). A representation of the etched feature is shown in the right hand side of Fig. 2.10.

Several steps were used to form the active layer of the PMC. The protective layer

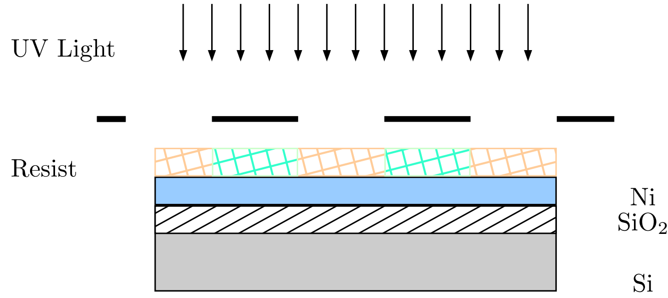

Figure 2.9: First lithography mask exposure to create cathode bar.

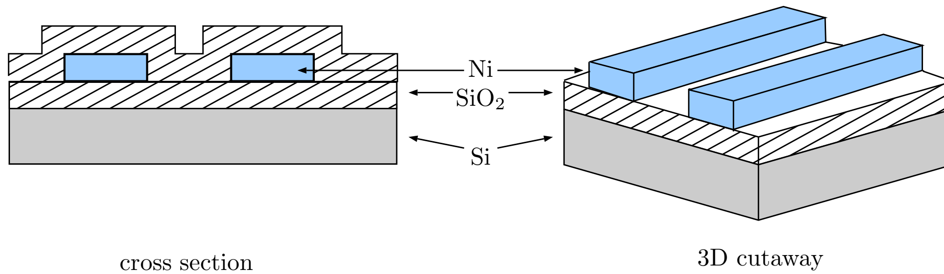

Figure 2.10: Ni layer wet etched to create cathode bar followed by deposition of SiO_2.

of resist was removed by soaking the wafer in acetone followed by a rinsing of isopropyl alcohol (IPA). After the resist was removed, the wafer was placed back into the Lesker PVD75 electron beam evaporator, pumped down to high vacuum, and a 100 nm layer of SiO_2 deposited at 0.9 Å/s. The wafer was removed from the vacuum chamber and another layer of AZ3312 resist spun on with the same recipe as described previous. Crossbar mask #2 was used to pattern (Fig. 2.11) the resist, this time with vias used for holding the active device layer. The vias shown in Fig. 2.12 were etched through the SiO_2 layer with 100 mL buffered oxide etch (BOE) solution after ten minutes. The resist for the etch mask was removed with acetone and another layer of resist, this time AZ4330, was spun on at 2000 RPM for 30 seconds. The resist was soft

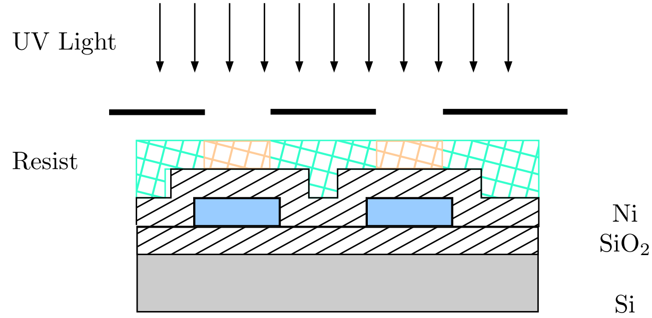

Figure 2.11: Second lithography mask to etch via through SiO_2.

baked at 100°C before undergoing lithography with crossbar mask #3 in the EVG to a 300 mJ/cm^2 UV exposure. This lithography step is depicted in Fig. 2.13. The resist was developed for two minutes using AZ 300 MIF. The wafer was placed into a Cressington 308R thermal evaporator where, as shown in Fig. 2.14, 60 nm of $Ge_{30}Se_{70}$ was deposited followed by 30 nm Ag. As shown in Fig. 2.15, the $Ge_{30}Se_{70}$ layer was photo-doped with the Ag by exposing the device side (top) of the wafer to UV ($\lambda =$ 324 nm) light for one hour. The importance of the Ag doping concentration will be discussed in the next section. After the photo-doping process, the wafer was placed back into the Cressington evaporator where 35 nm of additional Ag was deposited to form the top active metal anode. Fig. 2.16 shows the device structure after the resist is dissolved, lifting off the chalcogenide and electrode layers around the individual device vias.

The final steps create the Al crossbar contacts across the anode of the devices. The wafer was again coated in AZ4330, spun on at 2000 RPM for 30 seconds. The resist was soft baked at 100°C for 60 seconds. Crossbar mask #4 was used to image a lift-off layer for the Al contacts, using the EVG for a UV exposure to 300 mJ/cm^2. The wafer was placed in the Lesker electron beam evaporator where 400 nm of Al was deposited at 1 Å/s. The resist layer was dissolved in acetone to lift-off the excess Al, leaving behind dog bone style contacts. Another layer of AZ4330 resist was laid

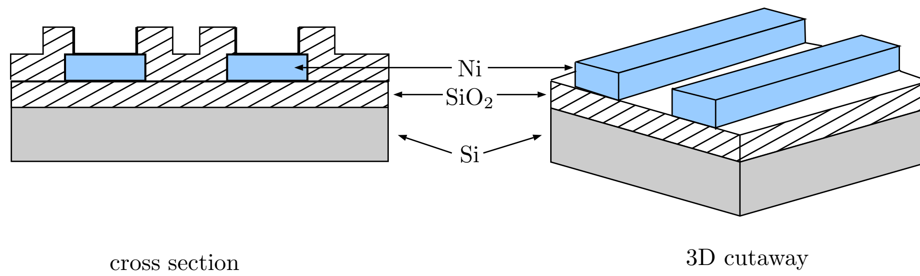

Figure 2.12: Vias wet etched through SiO_2 to Ni layer.

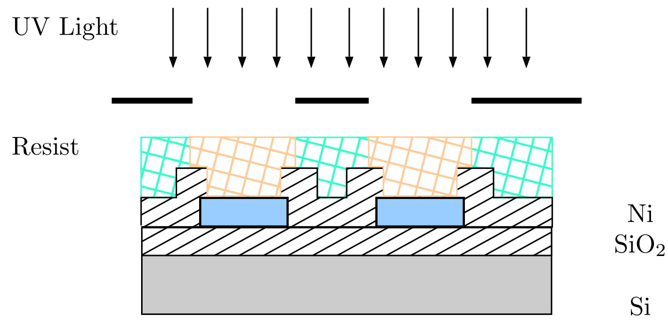

Figure 2.13: Third lithography mask for device layer lift-off.

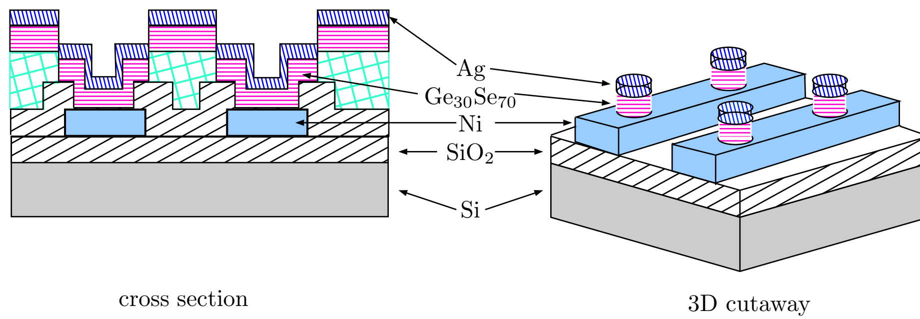

Figure 2.14: $Ge_{30}Se_{70}$ is deposited followed by Ag.

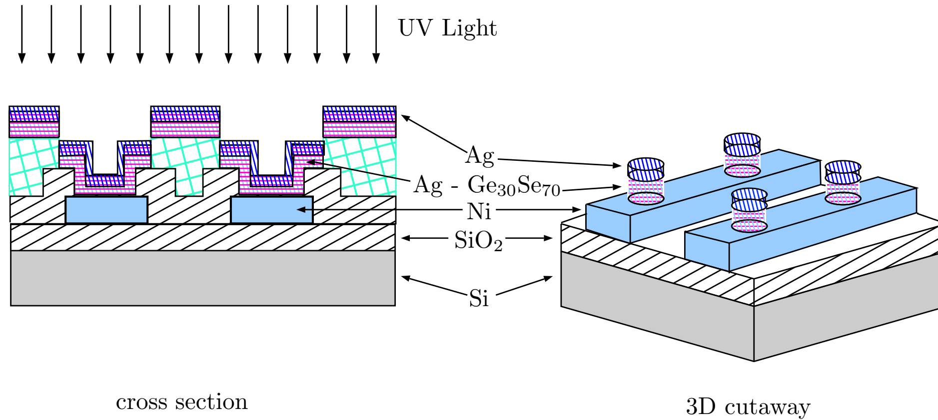

Figure 2.15: $Ge_{30}Se_{70}$ is photo-doped with Ag by exposing to UV light.

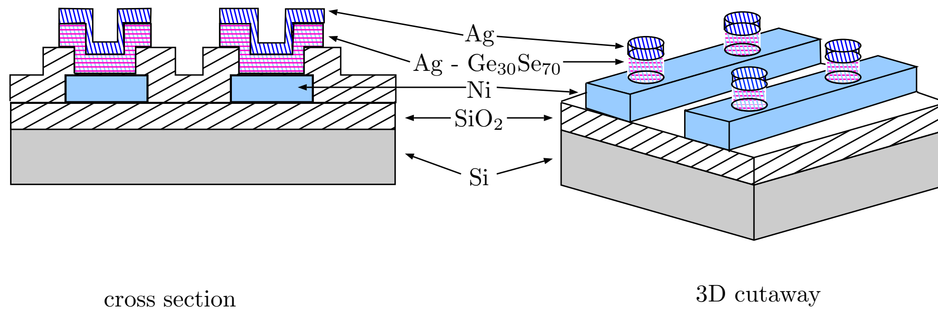

Figure 2.16: Additional Ag is deposited then the wafer is soaked in acetone to remove the resist and lift-off the excess material.

down in the manner described for the Al lift-off layer. The final mask #5 was used to image contact pads over both ends of the dog bone electrodes (both anode and cathode contacts). The purpose of this layer was to apply a thicker layer of metal where probing and wire bonding may take place. The wafer was placed back into the Lesker one final time, to deposit an additional 400 nm of Al at 1.5 Å/s. After deposition, the resist was removed with acetone to lift-off the Al. To finish the devices, the wafer was annealed at 120°C for 20 minutes. Fig. 2.17 depicts the complete layer stack of the PMC. A picture of the finished crossbar structure is shown in Fig. 2.18.

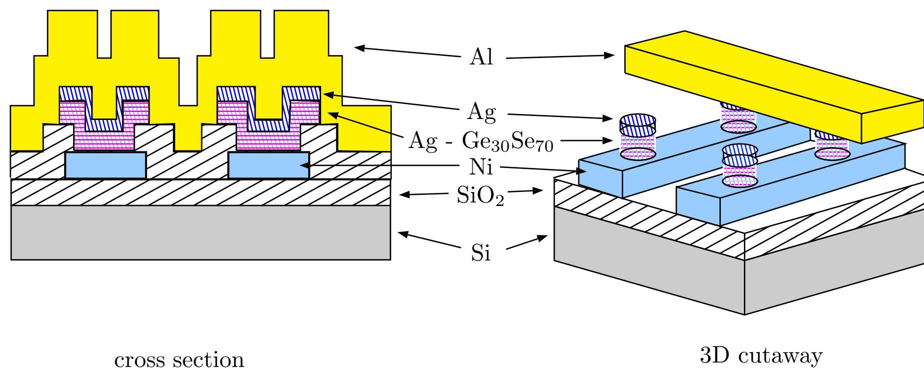

Figure 2.17: Al is deposited and lifted off to create top anode crossbar.

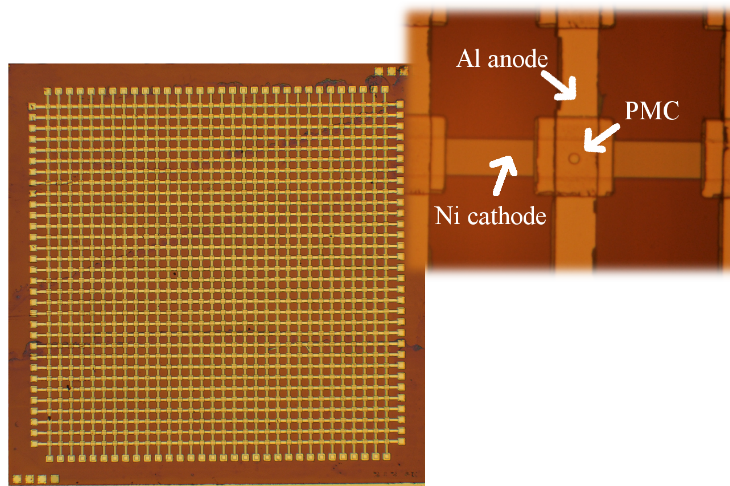

Figure 2.18: Fabricated crossbar tile. Zoomed image highlights the device contacts and active device region.

2.6 Ag Doping Profile in PMC Structures

During the fabrication of the devices, the ChG layer is photo-doped with approximately 33 at.% concentration of Ag. The 33 at.% concentration has been shown to be the saturation point for Ag diffusion into $Ge_{30}Se_{70}$ [18]. When Ag diffuses into $Ge_{30}Se_{70}$, the material becomes denser as the Ag fills porous regions throughout the ChG, preventing further diffusion of Ag [35]. It is expected that by saturating the ChG with Ag, diffusion of Ag away from a formed CF would be heavily limited. Simulated models have investigated the roll the Ag doping profile has on PMC properties

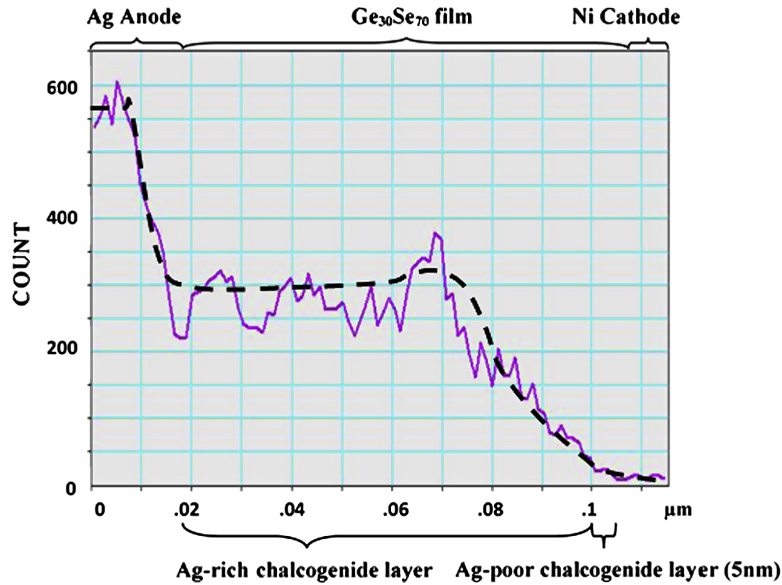

Figure 2.19: EDS data showing the profile of Ag throughout a PMC [37]. The purple solid line is the measured count while the dashed black line is the smoothed profile of the Ag count. Reprinted from Solid-State Electronics ©(2015), with permission from Elsevier.

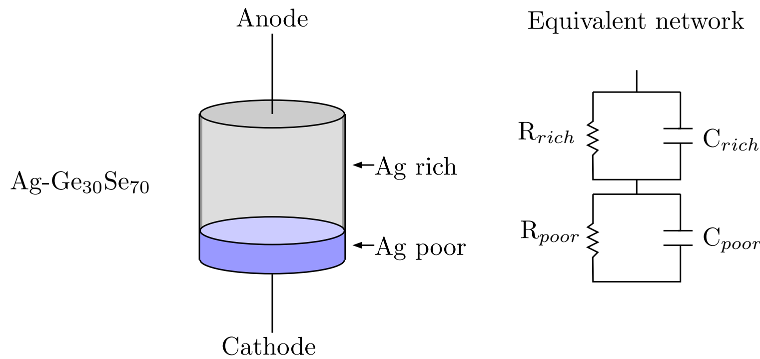

Figure 2.20: Ag doping regions in the $Ge_{30}Se_{70}$ layer (left) with the equivalent RC circuit network (right).

[36], [37].

In the work presented in [36] and [37], the photodoped ChG layer is shown to have two distinct regions in Fig. 2.19 and Fig. 2.20. The region nearest to the Ag anode is Ag rich. The region nearest the inert cathode is Ag poor. Impedance spectroscopy also provides evidence of the existence of these two regions [37], [38]. Electron Dispersive Spectroscopy (EDS) performed on HRS samples, shown in Fig.

2.19, shows the Ag rich region has an Ag concentration near the saturation limit (33 at.%) and the Ag poor region contains less than 10 at.% of Ag. It is not fully understood why the Ag poor region exists. It is speculated that the Ag poor region contains less Se than the rich region, making it more difficult for Ag to diffuse through. The Ag poor region plays an important roll in defining the HRS. The difference in affinity of the two regions creates a barrier at the interface of the two regions, resulting in a high resistance across the device [36].

Chapter 3

IONIZING RADIATION EFFECTS

3.1 Ionizing Radiation Effects in Semiconductors

Ionizing radiation can be in the form of high energy photons, electrons, protons, or heavy ions. When a high energy particle interacts with a material, a portion of the energy from the incident particle is transfered to the electrons in the atoms, ionizing the material. Ionization due to photons can occur in one of three processes, photoelectric effect, Compton scattering, or pair production. In the photoelectric effect, an incident photon is completely absorbed by an atom, ejecting an electron. In Compton scattering, a portion of the incident photon's energy is absorbed by an ionized electron and the remaining photon energy is emitted at some angle away from its original trajectory. Pair production requires higher energy photons than in the photoelectric effect or Compton scattering. During pair production, an incident photon interacts with an atom to create an electron-positron pair [39].

During ^{60}Co γ-ray irradiation of semiconductors, the high energy photons interact with the material to ionize an electron into the conduction band, leaving behind a hole in the valance band. In the presence of an electric field, the electron hole pair (ehp) can separate, with the electrons drifting toward the positive contact and the holes drifting to the negative contact. The rate G at which the generation of ehp occurs is given in equation (3.1). The generation rate is dependent on the dose rate $\dot{D}$, density ρ of the semiconductor, and the photon energy required to ionize an electron E_p. The ionization energy is approximately twice that of the band gap energy E_g.

Table 3.1: Material Parameters Used to Model PMC

ρ (ChG)	E_g (ChG)	μ_N	μ_P	ϕ_m(Ag)	ϕ_m(Ni)
7 g/cm^3	1.86 eV	10^{-5} $cm^2/(Vs)$	10 $cm^2/(Vs)$	4.29 V	5.15 V

$$G = \frac{\dot{D}\rho}{E_p} \tag{3.1}$$

In this thesis, two dose rates where tested, 8.8 rad(Si)/s and 210 rad(Si)/s. Using equation (3.1) and the parameters listed in Table 3.1, the generation rate for each of these dose rates is listed in Table 3.2.

Table 3.2: Dose Rates and Equivalent Generation Rates

$\dot{D}$ (rad(Si)/s)	G (cm^{-3}s^{-1})
8.8	1.0 $\times 10^{15}$
210.0	2.5 $\times 10^{16}$

3.2 Effect of the Electric Field on PMC Retention

To understand how ionizing radiation may affect a PMC, a look at the forces acting upon the device is needed. Due to the difference in the metal work functions (ϕ_m) of the anode and cathode contacts, there is an electric field across the ChG layer as shown in Fig. 3.2. The metal work functions are listed in Table 3.1. In the LRS, two forces act upon the CF, outward diffusion of Ag away from the filament and drift of the Ag toward the CF, as depicted in Fig. 3.1. The diffusion force is highly limited by the Ag doping saturation, as discussed in the previous chapter. To disturb the CF, the electric field would need to be disturbed in such a way as to increase the field above some threshold to allow Ag migration to the CF, or decrease or reverse the electric field such that Ag ions drift away from the CF and increase the resistance.

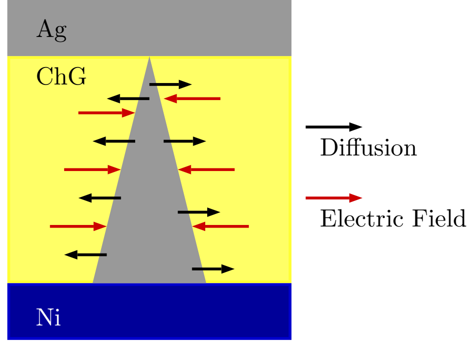

Figure 3.1: Forces acting upon the filament.

Since ehp generation in the ChG layer is the main response to ionizing radiation, technology computer aided design (TCAD) simulations were performed to evaluate how the electric field evolves with increasing generation rate.

To model the evolution of the electric field within a PMC, the parameters defined in Table 3.1 were used. In this two dimensional simulation, diffusion forces are considered negligible, so only the intrinsic electric field due to work function differences is considered. In the HRS scenario, no continuous path of Ag exists, so the electric field is similar to that shown in Fig. 3.2. During the LRS, a CF can be modeled with a triangular like shape [27]. Due to limitations of the TCAD model, to calculate the electric field the CF cannot touch the Ag contact. To model the LRS, a small gap was placed between the Ag contact and the tip of the CF.

The steady-state simulation results in Fig. 3.2 and Fig. 3.3 show how the magnitude of the electric field, along the defined cut lines, evolves with an increase in ehp generation rate. These results show that as the generation rate increases, the electric field begins to distort, weakening in the center of the ChG layer and strengthening at the Ag contact. This distortion is due to the separation of electrons and holes in the presence of a field. The lower generation rate of 10^{21} cm^{-3}s^{-1} shows no changes in the electric field due to irradiation. Both generation rates shown in Table 3.2 are below 10^{21} cm^{-3}s^{-1} and will therefore not significantly perturb the electric field.

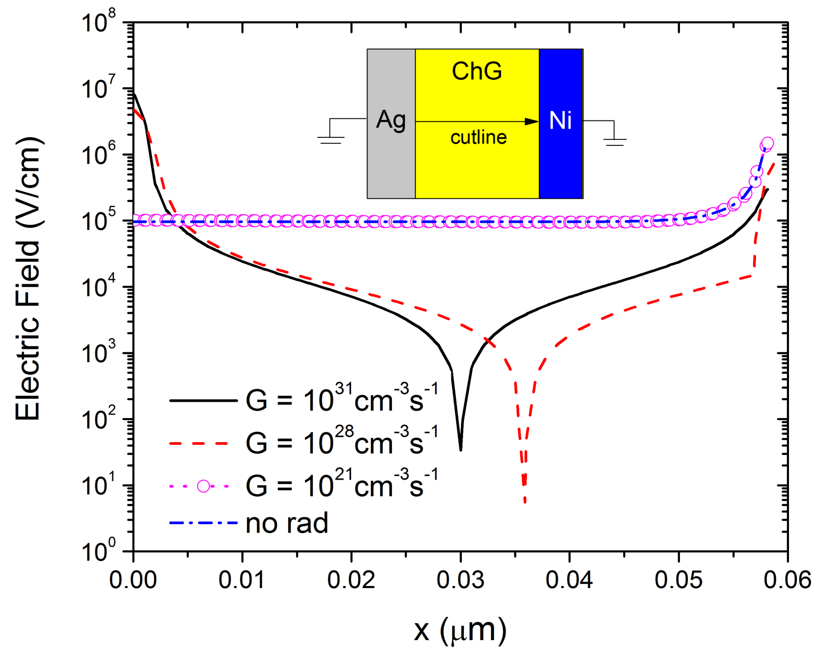

Figure 3.2: Electric field through a PMC in HRS for multiple generation rates.

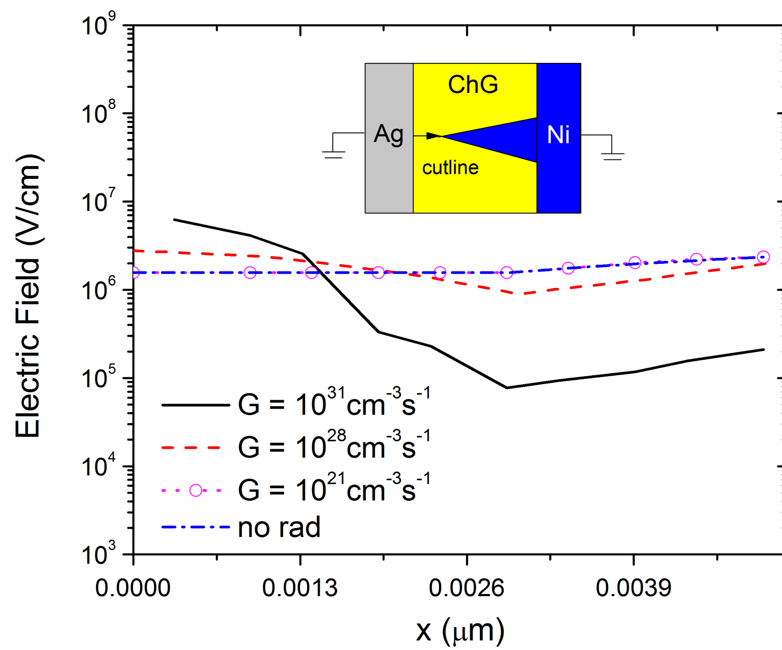

Figure 3.3: Electric field through a PMC in LRS for multiple generation rates.

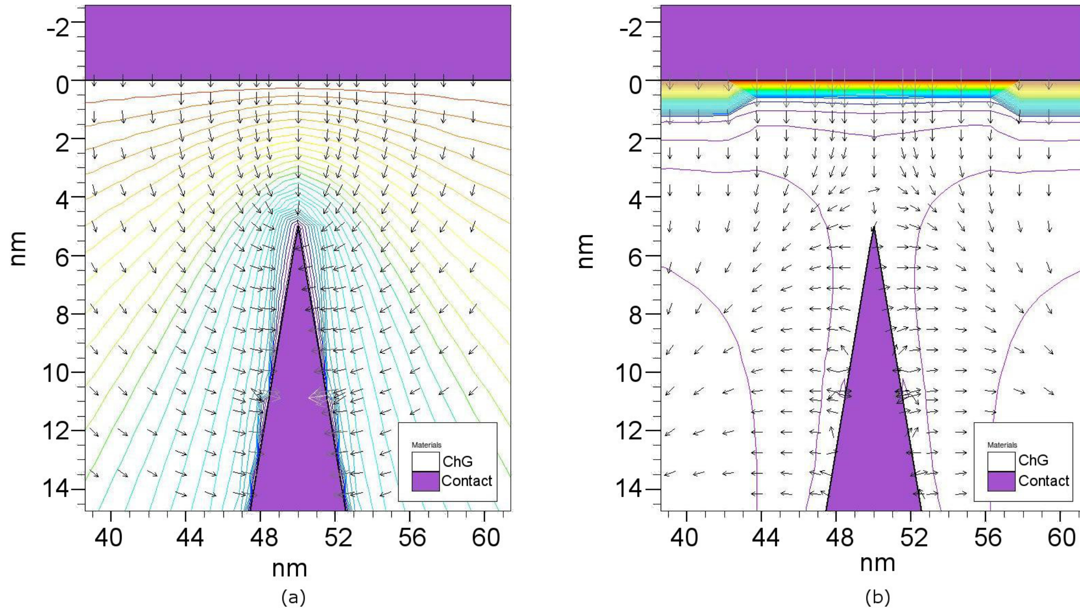

Figure 3.4: Equal potential and electric field vectors for the LRS during a) no irradiation and b) irradiation with a generation rate of 10^{31} cm^{-3}s^{-1}.

For the HRS, the electric field is equivalent for any cut line going from the Ag contact to the Ni contact. The electric field for the LRS is a bit more complex, as shown in Fig. 3.4 and Fig. 3.5. The electric field in Fig. 3.4 is shown to be approximately perpendicular to the filament surface. For the case of no radiation Fig. 3.4(a) shows the field directed toward the filament. During irradiation with a generation rate of 10^{31} cm^{-3}s^{-1}, Fig. 3.4(b) shows that the field inverts, directed away from the filament. These results imply that at a high dose rate, the filament may dissolve under the influence of the electric field.

The results in Fig. 3.2 and Fig. 3.3 imply that the dose rates tested in this thesis do not affect the electric field. To further demonstrate that dose rates below 210 rad(Si)/s do not affect the field, a generation rate of 10^{17} cm^{-3}s^{-1} was simulated in Fig. 3.5. No change to the electric is observed as compared to the no radiation environment shown in Fig. 3.4.

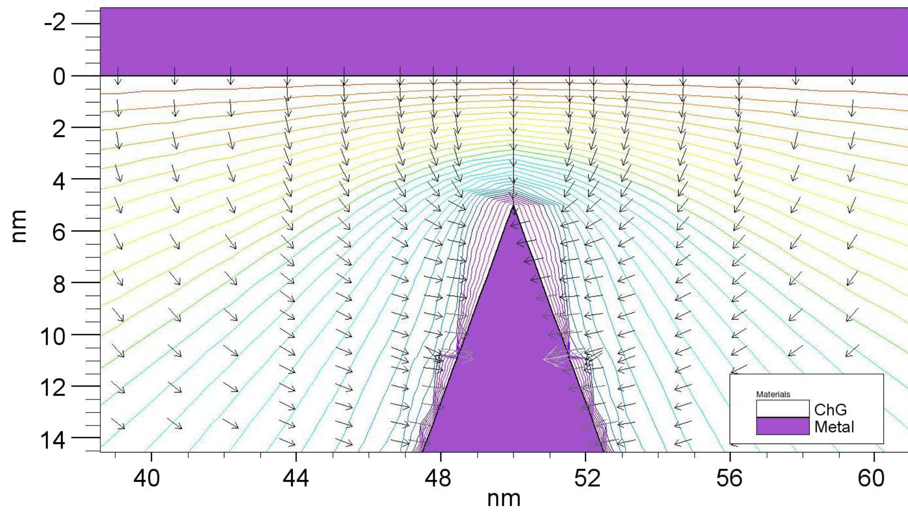

Figure 3.5: Equal potential and electric field vectors for a generation rate of $10^{17}\text{cm}^{-3}\text{s}^{-1}$.

Chapter 4

RETENTION DURING ^{60}Co γ-RAY EXPOSURE

4.1 State Retention During Ionizing Irradiation to 3.1 Mrad(Si)

Chapter 2 of this thesis has shown that PMC devices retain information in environments with no significant amount of ionizing radiation, with a projected retention of ten years [13],[33]. Special applications, such as use in sterilized medical devices, satellites, and other space-based electronics, require devices to be exposed to a high levels of ionizing radiation. This chapter of the thesis will explore the response of PMCs to a total ionizing dose. Specifically, this chapter will present data showing how PMC devices retain their programmed HRS or LRS state while being subjected to ionizing ^{60}Co γ-ray irradiation. Two different scenarios are explored. The first scenario studies devices exposed up to 3.1 Mrad(Si) while device pins were left floating. The second scenario features devices exposed, in one dose step, to 10.1 Mrad(Si) with a constant 50 mV bias applied to the anode while the cathode pins were grounded. This second scenario was performed with *in situ* measurement, allowing any changes in resistance state to be observed real time.

All devices tested were fabricated using the method detailed in Chapter 2. Several device tiles were packaged into 28-pin ceramic dual in-line packages (CDIP), as shown in Fig. 4.1. Before exposure to radiation, each package was placed into an Agilent 16442B test fixture, as shown in Fig. 4.2, to conduct electrical characterization. Previous studies have highlighted the sensitivity of Ag doped Ge_xSe_{1-x} to light, especially in the UV band [40], [41]. During measurements, the lid of the test fixture remained closed to ensure that light did not affect the measured current-voltage (I-V)

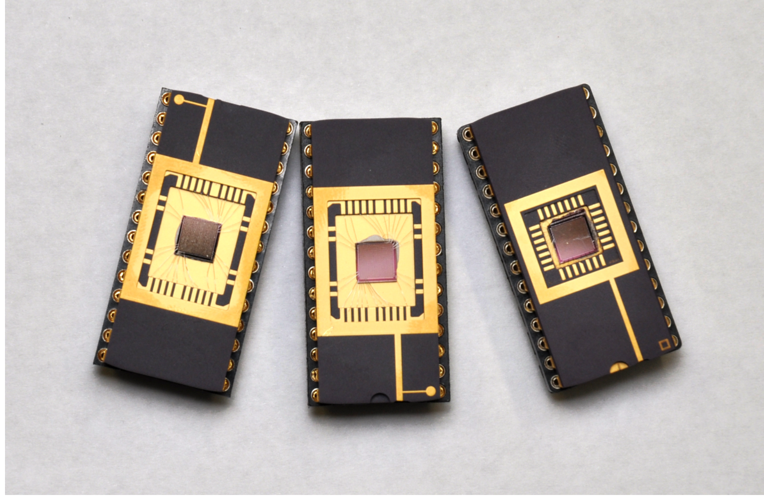

Figure 4.1: Crossbar device tile wire bonded into a 28-pin CDIP.

characteristics. The inputs of the text fixture were connected via low noise triaxial cables to the source measurement unit (SMU) outputs of an Agilent 4156C parameter analyzer. To perform an I-V measurement, the SMU connected to the cathode of a PMC device was set to a constant common ground output while the SMU connected to the anode was swept from 0 V to 0.5 V then back to 0 V in steps of 10 mV. The positive voltage sweep results in the I-V characteristic for programming the PMC device to a LRS. The LRS can be controlled by defining a compliance current on the parameter analyzer. The greater the compliance current value, the lower the LRS will be [26]. To obtain the I-V characteristics for dissolving or *erasing* the filament, the anode is instead swept between 0 V and -0.5 V. Each device considered for testing was swept approximately thirty times to verify its functionality and obtain statistics for the LRS and HRS conditions. This measurement process was automated using LabView to control the parameter analyzer and collect data.

Before exposing the devices, five devices were set to HRS and five others were programmed to LRS with an I-V sweep at a current compliance level of 1 μA. The 1 μA programming compliance resulted in a LRS of approximately 100 kΩ. After the devices were programmed, they were transported to the irradiation facility.

Figure 4.2: Test fixture used for performing automated electrical measurements.

Table 4.1: Radiation Dose Steps

Step Time (min)	Dose Step (rad(Si))	TID (rad(Si))
1523	8.075×10^5	8.075×10^5
1500	7.949×10^5	1.602×10^6
2934	1.555×10^6	3.158×10^6

The devices were exposed to ^{60}Co γ-ray irradiation in a Gammacell 220. The Gammacell used is shown in Fig. 4.3. The inner chamber of the Gammacell contains a ring of forty eight 21.11 *cm* tall *pencils*, each of which contains seven ^{60}Co slugs. Fig. 4.4 shows the source cage contained inside the Gammacell 220 [42]. Devices to be irradiated were loaded into a sample chamber at the bottom of the shielding plug. When the plug is lowered into the chamber, the sample chamber is positioned at the center of the source ring.

Fig. 4.5 shows the exposure board with drawn on dose contour. The packaged devices were placed in the sockets along the center most contour to maintain equivalent exposure. The board was placed onto a wooden stand to hold the board during

Figure 4.3: The Gammacell 220 used for γ-ray exposure. Photo provided by Dr. Keith Holbert.

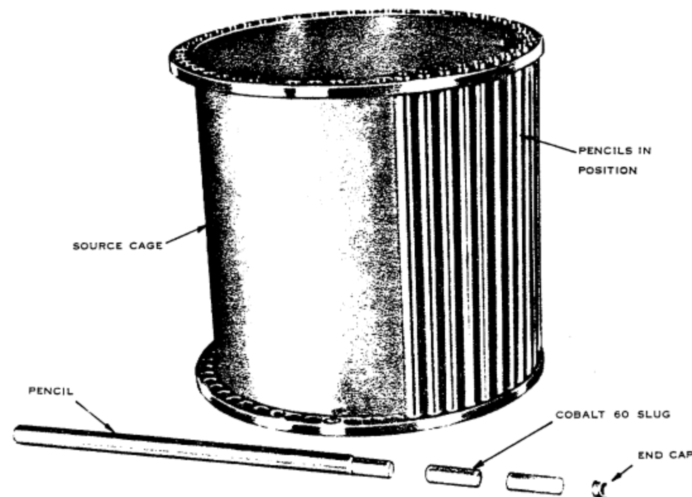

Figure 4.4: The source ring inside the central chamber of the Gammacell 220, as depicted in the Gammacell 220 instruction manual [42].

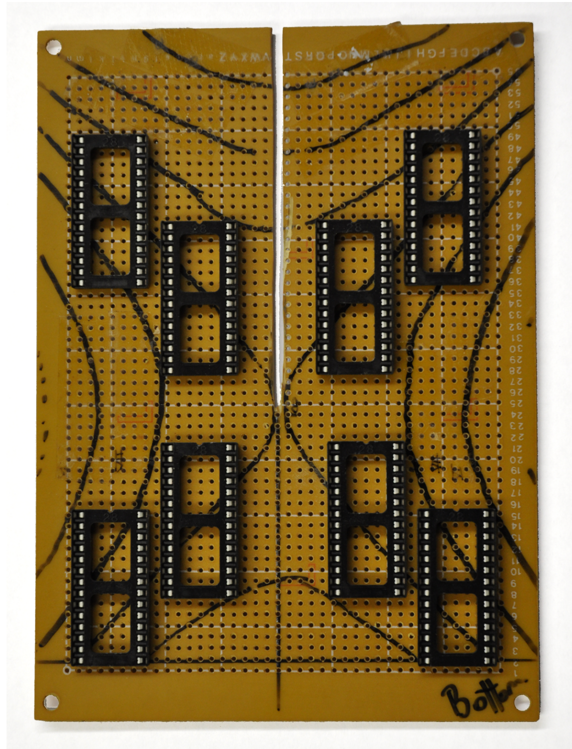

Figure 4.5: Board with marked dose contours of the Gammacell 220 chamber.

irradiation. The sample chamber was lowered into the Gammacell and left for exposure for the time steps listed in Table 4.1. The device pins for this test were left floating during irradiation. At the end of each dose, the packages were removed from the chamber, placed inside a light tight box, and transferred to the lab to sample the resistance state of each device. The resistance state was sampled by applying a 10 mV signal to the anode. The samples remained outside of the irradiation chamber for less than two hours.

The control devices (not irradiated) were tested in a similar fashion to the devices irradiated. Due to a limitation of available parts, only four control devices were used. Two of the devices were erased into the HRS and two were programmed to LRS using a DC sweep with a compliance current of 1 μA. Measurements on the control parts were performed in the same test fixture. Every 24 hours, the resistance state of the control devices were sampled. Once the measurements were completed, the device

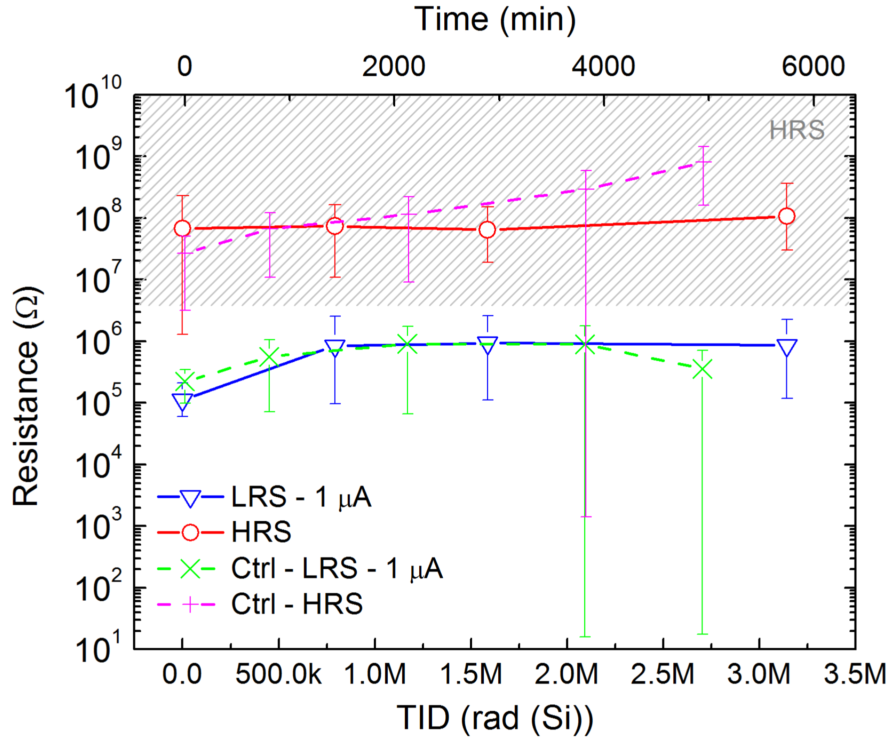

Figure 4.6: Retention of PMC devices during ionizing γ-ray irradiation to a TID of 3.1 Mrad(Si).

package was removed from the test fixture and placed in the same light tight box used to house the irradiated parts during transfer between labs. The purpose of removing the control device from the test fixture was to mimic the treatment of the irradiated packages.

The results in Fig. 4.6 show that the irradiated PMC devices maintain their programmed state for the 3.1 Mrad(Si) TID. The gray cross hatched area defines the HRS region while the white region below is the LRS. The boundary between HRS and LRS was determined by calculating the median HRS value of the irradiated and control devices prior to irradiation. The irradiated devices programmed to a HRS are shown to be very stable with an average deviation of 24% from the initial state. The HRS control devices drifted to a higher resistance over time. Both the irradiated and control devices in the LRS are shown to drift to a higher resistance within the

first 1000 minutes of being programmed. After this initial drift, the devices remain at approximately 880 kΩ for the remainder of the test. During the four day duration of the test, the irradiated devices maintained a window between HRS and LRS of two orders of magnitude. Due to the limited number of devices tested, the error bars represent the spread of resistance values measured at each dose step instead of standard error. The control devices have less stable retention than the irradiated devices.

The TID retention results presented in 4.6 were performed on devices with contacts left floating during exposure. No significant effects were seen at a 3.1 Mrad(Si) exposure. The test presented in the next section will explore the retention behavior of biased devices.

4.2 State Retention During Ionizing Irradiation to 10.1 Mrad(Si)

The following experiments were performed at Sandia National Laboratories at the Gamma Irradiation Facility (GIF). The GIF features several dry-cell concrete rooms each with a unique ^{60}Co source to offer a wide variety of dose rates. The cells are several square meters, allowing for the radiation exposure rate to be controlled by varying the distance from the source. While not in use, the ^{60}Co source is lowered into a water pool, making it safe for humans to enter the irradiation cell. Fig. 4.7 shows the source ring raised out of its pool. The ^{60}Co source is similar in design to the source ring shown in Fig. 4.4. The cell chosen for use in the following irradiation experiment contained a source with dose rates appropriate for MIL-STD-883 method 1019.9 TID testing. The MIL-STD-883 testing standard provides a method of testing microelectronics for use in a space radiation environment.

The devices used for irradiation at the GIF were the cross bar structures described in Chapter 2, though from a batch different than those used in the previous section.

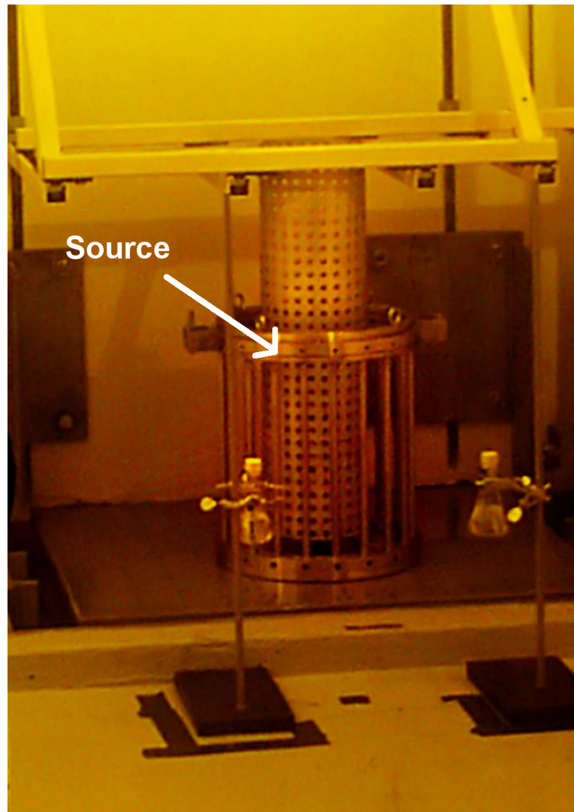

Figure 4.7: Dry-cell at GIF with raised ^{60}Co source ring. Original photo taken by Randy Montoya [43].

Two chips were packaged into 40 pin CDIP packages to allow for access of more devices than the 28 pin CDIP. Each chip contains 32 devices with 20 devices accessible. The devices were voltage swept between -0.5 V and 0.5 V approximately 30 times using an Agilent 4155B parameter analyzer controlled by LabView to verify device functionality.

The device package to be irradiated was placed onto a test board that allowed each pin to be accessed with a ribbon cable connection. Four thermoluminescent dosimeters (CaF_2 TLD) were placed at the top of the test board and another four at the bottom of the board, just below the package socket. The test board was placed inside a Pb/Al enclosure to shield the devices from low energy scattered radiation. The enclosure was suspended between two stands, as shown in Fig. 4.7, and oriented

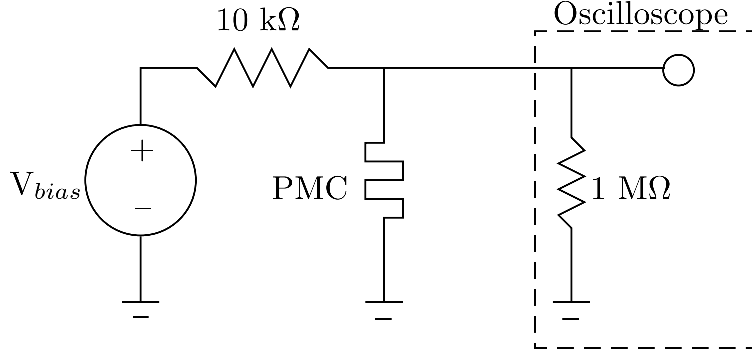

Figure 4.8: Circuit configuration used to actively monitor PMC devices.

such that the package-side of the board faced the source ring. The stands were placed on the lip of the pool to achieve a high dose rate. The dose rate inside the enclosure was measured at 210 rad(Si)/s.

Prior to radiation exposure, five devices were erased into a HRS and four were programmed to a LRS with a 100 μA compliance current using a Keithley 2450 SMU. A packaged tile of control devices was kept outside of the radiation cell. Two of the control devices were programmed to a LRS with a 100 μA compliance current while two other devices were erased to a HRS.

The configuration used to monitor both the irradiated devices and control devices is shown in Fig. 4.8. The devices inside the irradiation cell were individually accessed using two 60 ft ribbon cables connected to a printed circuit board (PCB) that converted the ribbon cable connections to BNC coaxial connections. Coaxial cables were connected from the PCB to individual inputs of a Yokogawa DL750 oscilloscope. The PCB used for accessing the control devices featured individual BNC connections for each pin of the device. The four control devices were also connected to the inputs of the oscilloscope. The remaining input was used to monitor the bias voltage applied to both the control and irradiated devices. During testing, a 50 mV read bias was applied to the circuit in Fig. 4.8.

The PMC devices were irradiated at 210 rad(Si)/s to a TID of 10.1 Mrad(Si).

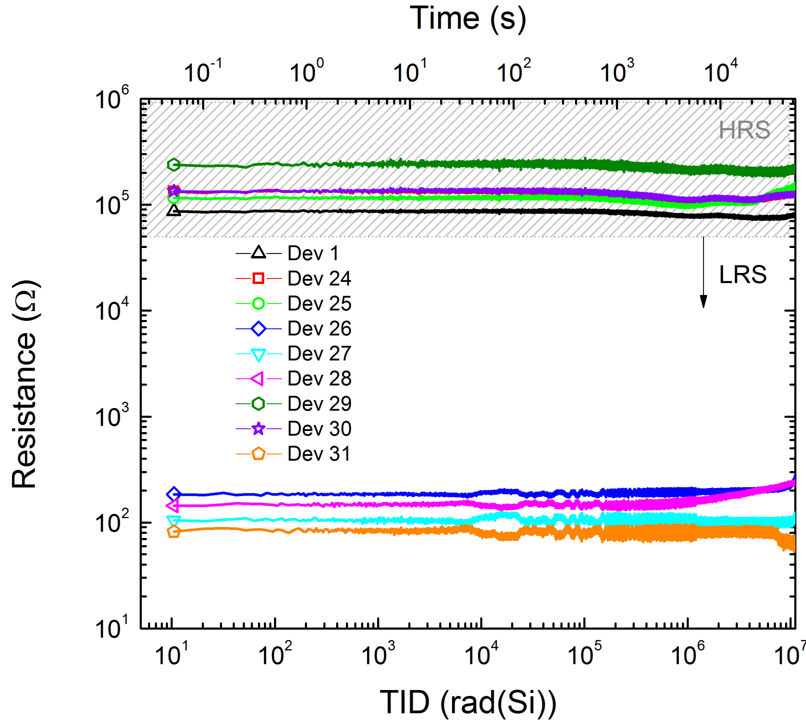

Figure 4.9: Retention of programmed resistances up to a TID of 10 Mrad(Si).

During irradiation, the resistance state of the devices were sampled continuously at a rate of 50 samples/s.

Using the configuration in Fig. 4.8, the voltage vs. time signal measured on the oscilloscope was converted to the resistance values. The resistance vs. time data of devices in the HRS and LRS conditions are shown in Fig. 4.9. The range of HRS data is marked on the plot with a gray hashed area. The minimum HRS data boundary is defined as the minimum observed value of the HRS while cycling the devices prior to irradiation (i.e., 50 kΩ). The HRS state is shown to be very stable for the entirety of the exposure. The plot in Fig. 4.10 highlights the HRS with the mean of the two HRS control devices marked with a dashed magenta line. The HRS of the exposed devices did not vary significantly during the exposure. The LRS is observed to be stable to a TID of 10.1 Mrad(Si).

One of the benefits of the PMC technology is the ability to reliably program a

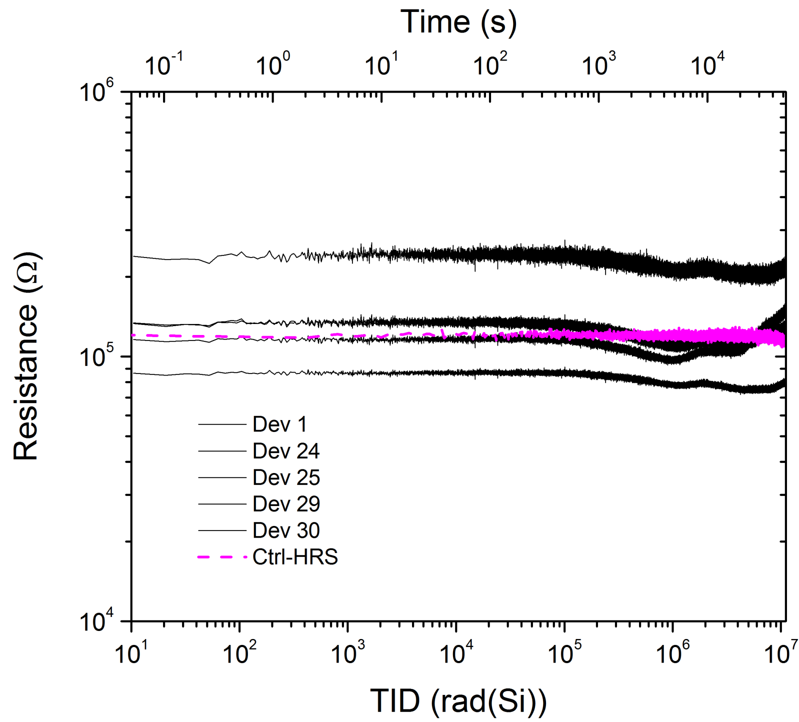

Figure 4.10: Retention of the HRS.

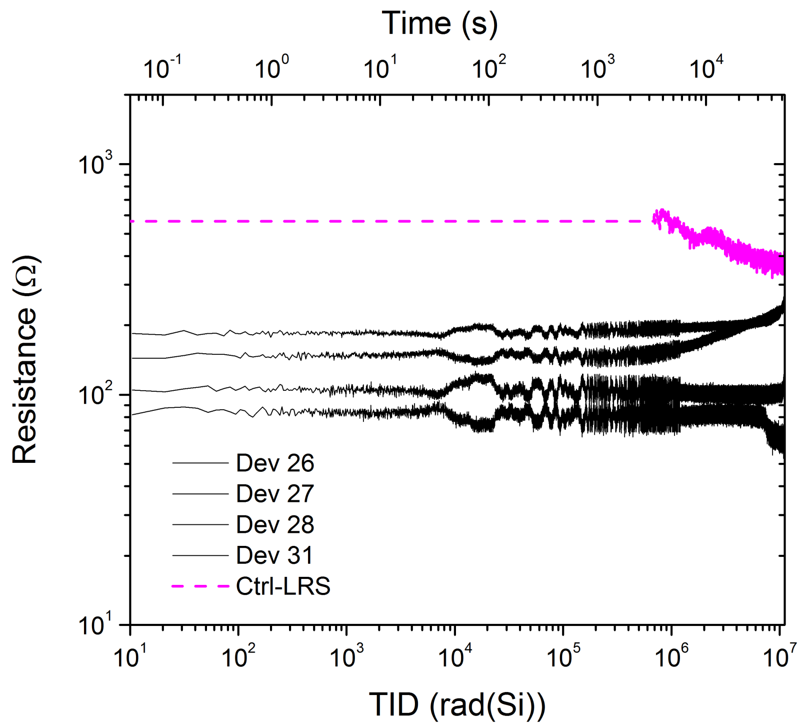

Figure 4.11: Retention of the LRS.

cell to multiple state levels [26], [29]. For this application to function correctly in a radiation environment, it will need to retain its state and not transition to a different logic defined resistance level. For the presented case of a 100 Ω resistance level, the PMC devices are shown to remain at their programmed level until the TID of 10.1 Mrad(Si). Other low resistance states will need to be observed to verify that multilevel program retention is possible in a radiation environment. In the previous chapter, it is shown that a device programmed with a 1 μA compliance current is capable of retaining the programmed state to a TID of 3.1 Mrad(Si). The capability of the high LRS state retaining its programming suggests that LRS retention between 100 kΩ and 100 Ω is likely.

4.3 Discussion and Analysis

Previous studies [40], [41] on the effects of ionizing irradiation have shown that irradiation can promote the diffusion of Ag into the ChG layer. As part of the photo-doping process, UV light exposure ionizes the Ag layer and encourages diffusion as well as chemical interaction with Se [44],[45]. If the γ-rays penetrate the metal contacts to interact with the filament itself, the Ag in the filament should become ionized and begin to diffuse into the surrounding ChG. The presented results in Fig. 4.6 show that for the LRS, when the CF is formed, the state follows the behavior of the control devices, suggesting that the Ag in the CF is not dissolving due to irradiation. The stability of the CF is likely due to the concentration gradient of the Ag doping in the ChG.

The TID PMC retention tests presented show promising retention results for PMC that would be exposed to high levels of ionizing radiation. Fig. 4.12 shows that the PMCs tested in this thesis exhibit a TID tolerance, several orders of magnitude higher than commercial NAND Flash devices. The retention data presented in Fig.

4.12 features the percent of errors observed per chip for NAND Flash 8 Gb single-level cell (SLC) and multi-level cell (MLC) [46], 32 Gb SLC [47], and a 64 Gb MLC [47]. The 8 Gb memory was fabricated at the 51 nm node and the 32 Gb and 64 Gb memory was fabricated at the 25 nm node. Each curve represents the average number of errors for three separate memory chips. The Flash chips were operated in No Refresh Mode, meaning that at the end of each dose step, the programmed state was read to determine the retention of the initial programmed state.

Preliminarily PMC devices are observed to have a greater tolerance to ^{60}Co γ-ray irradiation than NAND Flash devices, but the tens of devices tested in this thesis do not compare to the billions of memory cells tested on the Flash chips. To provide a better understanding of how ChG based PMC devices compare in performance to NAND Flash, results for a GeS_2 based 128 kb CBRAM chip from Adesto Technologies Corporation is marked as a gray dotted line [48]. The Adesto CBRAM devices function with the same mechanisms as the PMC devices presented [13]. No errors were found up to the maximum tested TID of 447 krad (GeS_2).

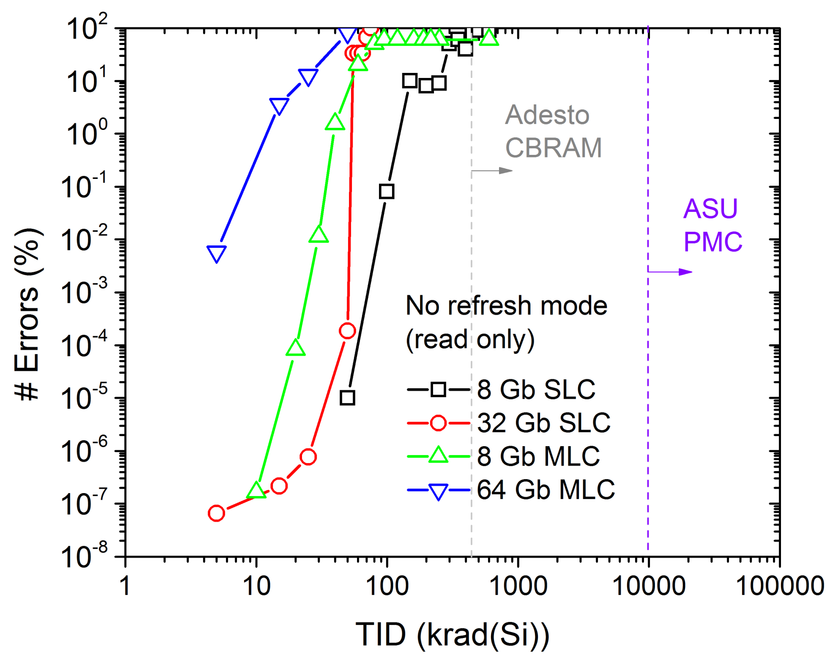

Figure 4.12: Percent errors as a function of TID in NAND Flash no refresh mode retention. Data obtained from [46],[47],[48].

Chapter 5

CONCLUSION

In this thesis, the effects of ionizing radiation on the retention of state in PMC devices was examined. Two different test setups were performed. In the first test, the devices were exposed to ^{60}Co γ-rays while the device contacts were left floating. The devices were exposed up to 3.1 Mrad(Si). In the second test, the devices were biased at the anode with a 50 mV read current during irradiation. The TID for the *in situ* test was 10.1 Mrad(Si). The devices used for each test where both of the same structure but from two separate fabrication batches. In both tests, the retention was seen to be excellent with very little observed effect due to irradiation.

For the 3.1 Mrad(Si) exposure, the devices left in a HRS were shown to remain in the HRS with very little deviation in resistance over time. The devices in the LRS were programmed with a 1 μA current. Both the irradiated and control devices in the LRS were shown to drift to a higher resistance within the first 1000 minutes of being programmed. After the increase in resistance, the devices remained at the higher value for the duration of the exposure. During the TID exposure to 10.1 Mrad(Si), the devices were monitored *in situ*. The trace data presented in Chapter 4 shows that the retention state of all exposed devices remained constant for the duration of the test.

One very noticeable difference between the devices used for the two tests is the observed HRS. The devices used for both tests were produced with the same recipe, using the same equipment and materials, but the devices used for *in situ* testing operated with a lower HRS. Given the examination in Chapter 2, the difference in the HRS may be due to a difference in Ag doping profiles. Regardless of the reason

for the difference, devices from both batches worked correctly and were capable of retaining their programmed resistance state.

The ChG PMCs have been shown to be superior to commercial NAND Flash devices in terms of tolerance to ionizing radiation. The PMC devices retained their state up to 10.1 Mrad(Si) whereas the Flash devices are shown to fail after 300 krad(Si) or less. The presented comparison shows that PMC memory would be an excellent alternative to Flash for extreme radiation environments such as space or γ-ray sterilized medical devices.

REFERENCES

[1] T. Perry. (2014, Aug.) Soon to join the internet of things: the quantified cup. [Online]. Available: http://spectrum.ieee.org/view-from-the-valley/consumer-electronics/portable-devices/soon-to-join-the-internet-of-things-the-quantified-cup

[2] Fitbit is a registered trademark and service mark of fitbit, inc. [Online]. Available: http://www.fitbit.com/

[3] Vessyl is a trademark of mark one lifestyle, inc. [Online]. Available: https://www.myvessyl.com/

[4] Glass is a registered trademark of google inc. [Online]. Available: https://www.google.com/glass/start/

[5] Nest is a registered trademark of nest labs inc. [Online]. Available: https://www.nest.com/

[6] Nike is a registered trademark of nike inc. [Online]. Available: https://www.nike.com/

[7] International technology roadmap for semiconductors 2013. [Online]. Available: http://www.itrs.net/

[8] K. Strauss and D. Burger, "What the future holds for solid-state memory," *IEEE Computer*, vol. 47, no. 1, pp. 24–31, 2014.

[9] M. N. Kozicki and M. Mitkova, "Mass transport in chalcogenide electrolyte films materials and applications," *J. Non-Cryst. Solids*, vol. 352, pp. 567–577, March 2006.

[10] M. N. Kozicki, M. Park, and M. Mitkova, "Nanoscale memory elements based on solid-state electrolytes," *IEEE Trans. Nanotechnol*, vol. 4, pp. 331–338, May 2005.

[11] CBRAM is a registered trademark of Adesto Technologies Corporation. [Online]. Available: http://www.adestotech.com/products/cbram/

[12] I. Valov, R. Waser, J. R. Jameson, and M. N. Kozicki, "Electrochemical metallization memories-fundamentals, applications, prospects," *Nanotechnology*, vol. 22, no. 25, p. 254003, Jun. 2011, 2011.

[13] C. Gopalan, Y. Ma, T. Gallo, J. Wang, E. Runnion, J. Saenz, F. Koushan, P. Blanchard, and S. Hollmer, "Demonstration of conductive bridging random access memory (CBRAM) in logic CMOS process," *Solid-State Elec.*, vol. 58, no. 1, pp. 54–61, 2011.

[14] B. J. Lambert and J. M. Hanson, "ISO radiation sterilization standards," *Radiat. Phys. Chem.*, vol. 52, no. 1, pp. 11–14, 1998.

[15] R. Waser, R. Dittmann, G. Staikov, and K. Szot, “Redox-based resistive switching memories nanoionic mechanisms, prospects, and challenges,” *Adv. Mater.*, vol. 21, pp. 2632–2663, 2009.

[16] C. Schindler, S. C. P. Thermadam, R. Waser, and M. N. Kozicki, “Bipolar and unipolar resistive switching in Cu-doped SiO_2,” *IEEE Trans. Electron Devices*, vol. 54, no. 10, pp. 2762–2768, October 2007.

[17] M. N. Kozicki, C. Gopalan, M. Balakrishnan, M. Park, and M. Mitkova, “Non-volatile memory based on solid electrolytes,” *Proc. NVMTS*, pp. 10–17, 2004.

[18] M. Mitkova and M. N. Kozicki, “Silver incorporation in GeSe glasses used in programmable metallization cell devices,” *J. Non-Cryst. Solids*, vol. 299-302, no. 2, pp. 1023–1027, April 2002.

[19] C. Schindler, M. Meier, R. Waser, and M. N. Kozicki, “Resistive switching in Ag-Ge-Se with extremely low write currents,” *Proc. NVMTS*, pp. 82–85, November 2007.

[20] M. N. Kozicki, M. Balakrishnan, C. Gopalan, C. Ratnakumar, and M. Mitkova, “Programmable metallization cell memory based on Ag-Ge-S and Cu-Ge-S solid electrolytes,” *Proc. NVMTS*, p. 8389, 2005.

[21] M.-J. Lee, C. B. Lee, D. Lee, S. R. Lee, M. Chang, J. H. Hur, Y.-B. Kim, C.-J. Kim, D. H. Seo, S. Seo, U.-I. Chung, I.-K. Yoo, and K. Kim, “A fast, high-endurance and scalable non-volatile memory device made from asymmetric Ta_2O_5,” *Nature Mater.*, vol. 10, pp. 625–630, July 2011.

[22] B. J. Choi, D. S. Jeong, S. K. Kim, C. Rohde, S. Choi, J. H. Oh, H. J. Kim, C. S. Hwang, K. Szot, R. Waser, B. Reichenberg, and S. Tiedke, “Resistive switching mechanism of TiO_2 thin films grown by atomic-layer deposition,” *J. Appl. Phys.*, vol. 98, 2005.

[23] K.-L. Lin, T.-H. Hou, J. Shieh, J.-H. Lin, C.-T. Chou, and Y.-J. Lee, “Electrode dependence of filament formation in HfO_2 resistive-switching memory,” *J. Appl. Phys.*, vol. 109, p. 084104, 2011.

[24] A. L. Lacaita, A. Redaelli, D. Ielmini, F. Pellizzer, A. Pirovano, A. Benvenuti, and R. Bez, “Electrothermal and phase-change dynamics in chalcogenide-based memories,” *IEDM Tech. Dig.*, pp. 911 – 914, December 2004.

[25] D. Mahalanabis, H. J. Barnaby, M. N. Kozicki, V. Bharadwaj, and S. Rajabi, “Investigation of single event induced soft errors in programmable metallization cell memory,” *IEEE Trans. Nucl. Sci.*, vol. 61, no. 6, pp. 3557–3563, December 2014.

[26] U. Russo, D. Kamalanathan, D. Ielmini, A. L. Lacaita, and M. N. Kozicki, “Study of multilevel programming in programmable metallization cell (PMC) memory,” *IEEE Trans. Electron Devices*, vol. 56, no. 5, pp. 1040–1047, May 2009.

[27] S. Yu and H. S. P. Wong, "Compact modeling of conducting-bridge random-access memory (CBRAM)," *IEEE Trans. Electron Devices*, vol. 58, no. 5, pp. 1352–1360, May 2011.

[28] X. Guo, C. Schindler, S. Menzel, and R. Waser, "Understanding the switching-off mechanism in Ag+ migration based resistively switching model systems," *Appl. Phys. Lett.*, vol. 91, p. 133513, 2007.

[29] D. Mahalanabis, H. J. Barnaby, Y. Gonzalez-Velo, M. Kozicki, S. Vrudhula, and P. Dandamudi, "Incremental resistance programming of programmable metallization cells for use as electronic synapses," *Solid-State Elec.*, vol. 100, pp. 39–44, October 2014.

[30] J. L. Taggart, Y. Gonzalez-Velo, D. Mahalanabis, A. Mahmud, H. J. Barnaby, M. N. Kozicki, K. E. Holbert, M. Mitkova, K. W. an E. Deionno, and A. L. White, "Ionizing radiation effects on non-volatile memory properties of programmable metallization cells," *IEEE Trans. Nucl. Sci.*, vol. 61, no. 6, pp. 2985–2990, December 2014.

[31] B. Govoreanu and J. V. Houdt, "On the roll-off of the activation energy plot in high-temperature flash memory retention tests and its impact on the reliability assessment," *IEEE Electron Device Lett.*, vol. 29, no. 2, pp. 177–179, February 2008.

[32] W. Lee, J. Park, M. Son, J. Lee, S. Jung, S. Kim, S. Park, J. Shin, and H. Hwang, "Excellent state stability of Cu/SiC/Pt programmable metallization cells for nonvolatile memory applications," *IEEE Electron Device Lett.*, vol. 32, no. 5, pp. 680–682, May 2011.

[33] R. Symanczyk, R. Bruchhaus, R. Dittrich, and M. Kund, "Investigation of the reliability behavior of conductive-bridging memory cells," *IEEE Electron Device Lett.*, vol. 30, no. 8, pp. 876–878, August 2009.

[34] D. Kamalanathan, S. Balig, S. C. P. Thermadam, and M. Kozicki, "On state stability of programmable metalization cell (PMC) memory," *Proc. NVMTS*, pp. 91 – 96, November 2007.

[35] A. V. Kolobov and S. R. Elliott, "Photodoping of amorphous chalcogenides by metals," *Advances in Physics*, vol. 40, no. 5, pp. 625–684, 1991.

[36] M. Saremi, S. Rajabi, H. J. Barnaby, and M. N. Kozicki, "The effects of process variation on the parametric model of the static impedance behavior of programmable metallization cell (PMC)," *Mater. Res. Soc. Symp. Proc.*, vol. 1692, 2014.

[37] S. Rajabi, M. Saremi, H. J. Barnaby, A. Edwards, M. N. Kozicki, Y. Gonzalez-Velo, M. Mitkova, D. Mahalanabis, and A. Mahmud, "Static impedance behavior of programmable metallization cells," *Solid-State Elec.*, vol. 106, pp. 27–33, April 2015.

[38] Y. Gonzalez-Velo, H. J. Barnaby, M. N. Kozicki, and K. Holbert, "Total-ionizing-dose effects on the impedance of silver-doped chalcogenide programmable metallization cells," *IEEE Aero. Conf.*, pp. 1–7, March 2014.

[39] J. Schwank, "Basic mechanisms of radiation effects in the natural space environment," *1994 NSREC Short Course: Section II*, 1994.

[40] Y. Gonzalez-Velo, H. J. Barnaby, A. Chandran, D. R. Oleksy, P. Dandamudi, M. N. Kozicki, K. E. Holbert, M. Mitkova, M. Ailavajhala, and P. Chen, "Effects of cobalt-60 gamma-rays on Ge-Se chalcogenide glasses and Ag/Ge-Se test structures," *IEEE Trans. Nucl. Sci.*, vol. 59, no. 6, pp. 3093–3100, Dec. 2012.

[41] P. Dandamudi, M. N. Kozicki, H. J. Barnaby, Y. Gonzalez-Velo, M. Mitkova, K. E. Holbert, M. Ailavajhala, and W. Yu, "Sensors based on radiation-induced diffusion of silver in germanium selenide glasses," *IEEE Trans. Nucl. Sci.*, vol. 60, no. 6, pp. 4257–4264, Dec. 2013.

[42] *Instruction Manual Gammacell 220 Cobalt 60 Irradiation Unit*, 6th ed., Atomic Energy of Canada Limited, P.O. Box 93, Ottawa, Canada, July 1968.

[43] Randy Montoya, Sandia National Laboratory public released photograph. [Online]. Available: https://share.sandia.gov/news/resources/releases/2007/nanopart.html

[44] M. Mitkova, M. N. Kozicki, H. C. Kim, and T. L. Alford, "Local structure resulting from photo and thermal diffusion of Ag in GeSe thin films," *J. Non-Cryst. Solids*, vol. 338-340, pp. 552–556, 2004.

[45] T. Kawaguchi, S. Maruno, and S. R. Elliott, "Optical, electrical, and structural properties of amorphous AgGeS and AgGeSe films and comparison of photoinduced and thermally induced phenomena of both systems," *J. Appl. Phys.*, vol. 79, pp. 9096–9104, June 1996.

[46] F. Irom, D. N. Nguyen, R. Harboe-Srensen, and A. Virtanen, "Evaluation of mechanisms in TID degradation and SEE susceptibility of single and multi-level high density NAND flash memories," *IEEE Trans. Nucl. Sci.*, vol. 58, no. 5, pp. 2477–2482, October 2011.

[47] F. Irom, G. R. Allen, "Radiation Tests of Highly Scaled, High-Density, Commercial, Nonvolatile NAND Flash Memories-Update 2012," NASA JPL Publication 12-19 12/12. [Online]. Available: http://ntrs.nasa.gov/archive/nasa/casi.ntrs.nasa.gov/20140000667.pdf

[48] Y. Gonzalez-Velo, H. J. Barnaby, M. N. Kozicki, C. Gopalan, and K. E. Holbert, "Total ionizing dose retention capability of conductive bridging random access memory," *IEEE Electron Device Lett.*, vol. 35, no. 2, pp. 205–207, Feb. 2014.